

# Solar Neutrino Results from Super-Kamiokande

M. B. Smy

for the **Super-Kamiokande Collaboration**

*Department of Physics and Astronomy, 4182 Frederick Reines Hall,  
UC Irvine, California, USA*

Super-Kamiokande has measured the solar neutrino flux using elastic neutrino-electron scattering in water. The measured flux is  $2.32 \pm 0.03(\text{stat})^{+0.08}_{-0.07}(\text{syst}) \times 10^6 / (\text{cm}^2 \text{s})$  based on the energy range of 5 to 20 MeV for the recoiling electron. The time-dependence and energy spectrum of the recoiling electrons were studied to search for two-neutrino oscillation signatures. The absence of either significant zenith angle flux variation or distortions of the recoil electron spectrum places strong constraints on neutrino mass difference and mixing. In combination with the flux measurement, two allowed regions at large mixing are found.

## 1 Introduction

Using various detection methods, measurements of the solar neutrino flux<sup>1,2,3,4,5</sup> fall short of the flux predicted by the standard solar model<sup>6</sup> (SSM). This discrepancy is known as the “solar neutrino problem”. Neutrino flavor oscillations, similar to those seen in atmospheric neutrinos<sup>7</sup>, are a natural explanation for the discrepancy. In addition to a conversion in vacuum, a matter-induced resonance in the sun<sup>8</sup> may sufficiently enhance the disappearance probability of solar neutrinos even for small neutrino mixing. Matter effects can also modify the survival probability for neutrinos which pass through the earth<sup>9</sup>.

Super-Kamiokande (SK) is a 50,000 metric ton water Cherenkov detector. Solar Neutrinos are detected via elastic neutrino-electron scattering if the reconstructed energy of the recoiling electron is above 5 MeV. Vertex, direction and energy are reconstructed using the timing and pattern of the Cherenkov light produced by the recoil electron. About 11,000 photomultiplier tubes (PMTs) view the “inner detector”, a cylindrical volume containing 32,000 metric tons of water. Restricting the vertex of the solar neutrino event candidates to further than 2m from the PMTs leaves 22,500 tons of fiducial mass. Due to the energy threshold of 5 MeV, only the <sup>8</sup>B decay and the He—proton reaction (*hep*) branches of the solar neutrino spectrum are

accessible. To extract the solar neutrino flux from the sample of solar neutrino event candidates, the reconstructed direction of the recoiling electron is used (see<sup>5</sup> for details). The angle  $\theta_{\text{sun}}$  is defined as the angle between the reconstructed electron direction and the vector pointing from the sun to SK. In figure 1, the distribution of  $\cos(\theta_{\text{sun}})$  is shown. The strong correlation of the recoil electron direction with the neutrino direction leads to a clear peak at  $\cos(\theta_{\text{sun}})=1$ . Using 1258 days of data, the measured flux is (see figure 1)

$$\phi = 2.32 \pm 0.03(\text{stat})^{+0.08}_{-0.07}(\text{syst}) \times \frac{10^6}{\text{cm}^2\text{s}} \quad (1)$$

or  $45.1 \pm 0.5(\text{stat})^{+1.6}_{-1.4}(\text{syst})\%$  of the flux predicted by the BP2000<sup>6</sup> SSM.

The solar neutrino flux from the *hep* branch is expected to be about three orders of magnitude smaller than the <sup>8</sup>B branch. The endpoint of the *hep* spectrum (18.77 MeV) is higher than the <sup>8</sup>B spectrum endpoint (16 MeV). If the *hep* flux differs from expectation, the recoil electron spectrum will appear distorted. To place an upper limit on the *hep* flux, we define an energy range by maximizing sensitivity to *hep* neutrinos. The energy range chosen is 18 to 21 MeV. In this range we observe  $1.3 \pm 2.0$  solar neutrino events, or less than 3.9 events at 90% confidence level. From BP2000 ( $\phi_{\text{hep}} = 9.3 \cdot 10^3 / (\text{cm}^2\text{s})$ ) we expect  $0.9$  *hep* neutrinos, so 3.9 events correspond to an upper limit of the *hep* flux of  $40 \cdot 10^3 / (\text{cm}^2\text{s})$  at 90% confidence level (4.3 times the BP2000 prediction assuming no oscillation).

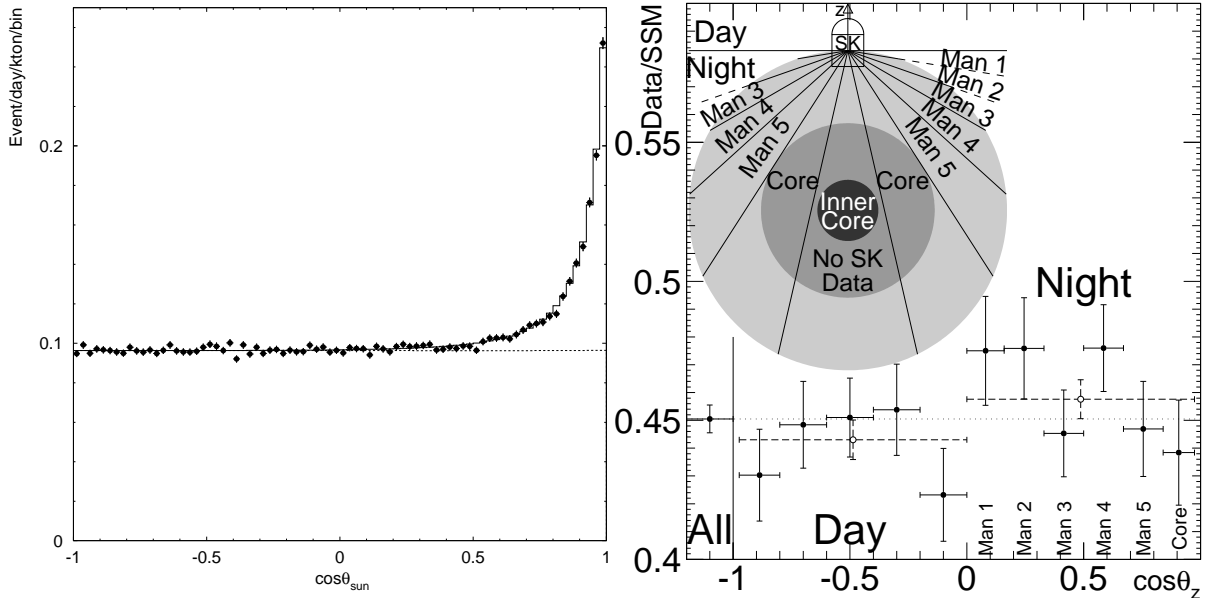


Figure 1: Angular distribution of solar neutrino event candidates (left) and solar neutrino flux in units of the flux expected from the BP2000<sup>6</sup> model (right). The strongly forward-peaked cross section of elastic neutrino-electron scattering leads to a clear peak of events pointing back to the sun. The recoil electron energy is limited between 5 and 20 MeV. Next to the total flux (45.1% BP2000; dotted line), the flux based on a day-time (night-time) sub-sample is shown (open circles; dashed line). The day-sample is further subdivided into five zenith angle bins, the night-sample into six (solid circles). Neutrinos in the last zenith angle bin pass through the core of the earth as indicated in the sketch of the earth's structure (right).

## 2 Time Variation of the Flux

We define the zenith angle  $\theta_z$  of an event as the angle between the vertical direction and the vector sun—SK at the time of the event. Day events have  $\cos \theta_z \leq 0$  and night events  $\cos \theta_z > 0$ .

Dividing the data into zenith angle bins, a flux is measured for each sub-sample. The resulting zenith angle distribution is shown in figure 1. It is consistent with a flat suppression of about 50% of the expected solar neutrino flux. To test the influence of the earth's matter density on the solar neutrino flux (a regeneration of the flux is predicted for some neutrino oscillation parameters) we construct the day–night asymmetry

$$A_{DN} = \frac{\phi_D - \phi_N}{\phi_{av}} \quad \text{where } \phi_{av} = \frac{1}{2} (\phi_D + \phi_N) \quad (2)$$

from the day flux  $\phi_D$  and the night flux  $\phi_N$ . This asymmetry is

$$A_{DN} = 0.033 \pm 0.022(\text{stat})^{+0.013}_{-0.012}(\text{syst}). \quad (3)$$

It is consistent with zero. Figure 2 shows the time variation of the solar neutrino flux. Each time bin extends over 1.5 months. No correlation with the sunspot activity was observed. Due to the eccentricity of the earth's orbit, the distance between sun and earth changes by about 3% with the season. As a consequence, a 7% annual modulation of the solar neutrino flux is expected. Some oscillation parameters predict a modification of this 7% modulation due to a change in the oscillation phase. To test this, the time bins are combined into 8 seasonal bins. The seasonal distribution is shown in figure 2. A  $\chi^2$  test including systematic uncertainties results in 3.8/7 degrees of freedom (for 7% modulation) compared to 8.1 (for flat). Therefore, a 7% annual modulation is favored over no modulation at the  $2\sigma$  level.

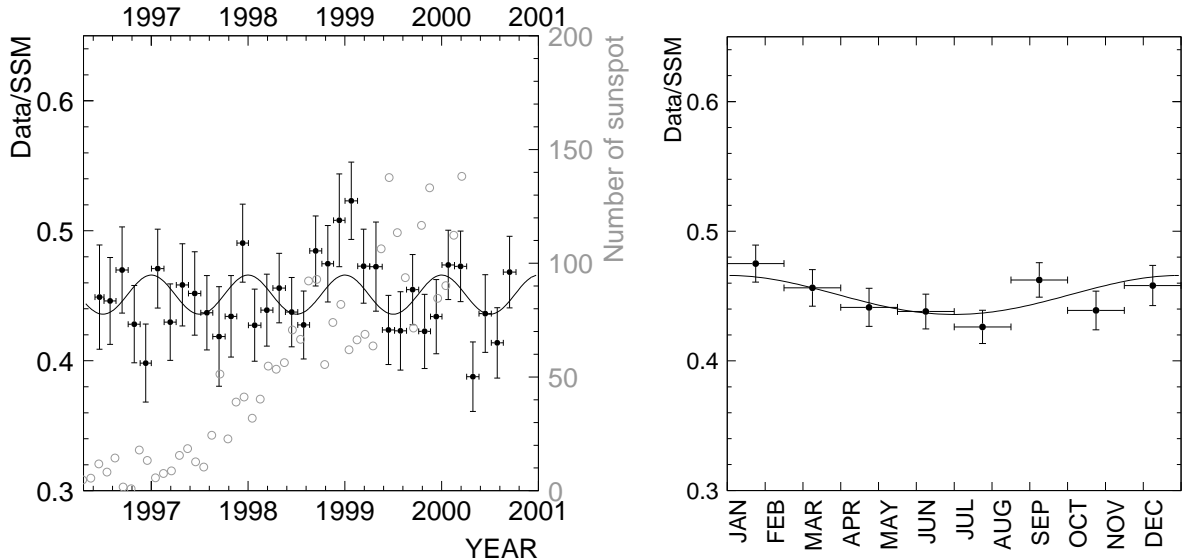


Figure 2: Time-dependence of the solar neutrino flux. Each data point extends over 1.5 months. No correlation with sunspot activity is observed. The solid line indicates the 7% annual modulation expected from the 3% change in distance between sun and earth. Combining the time bins into eight seasonal bins (right) the 7% modulation is favored by about  $2\sigma$  over a flat rate.

### 3 Neutrino Oscillation Search

In addition to suppression of the solar neutrino flux or modification of the seasonal dependence, neutrino oscillations can distort the neutrino spectrum (and therefore the recoil electron spectrum) or introduce zenith angle variations. To simultaneously study recoil electron spectrum and zenith angle dependence of the solar neutrino flux, the data are divided into energy bins

and zenith angle bins. SK defines eight energy bins and seven zenith angle bins (see figure 3). The size of each energy bin is about one standard deviation of the energy resolution function. Due to a statistical limitation, the data below 5.5 MeV and above 16 MeV are not broken into zenith angle bins. All other data are subdivided into six (about evenly-spaced) zenith angle bins for the night and one bin for the day. Solar neutrinos in the sixth night bin pass through the core of the earth. This way to bin the data is referred to as ‘zenith angle spectrum’.

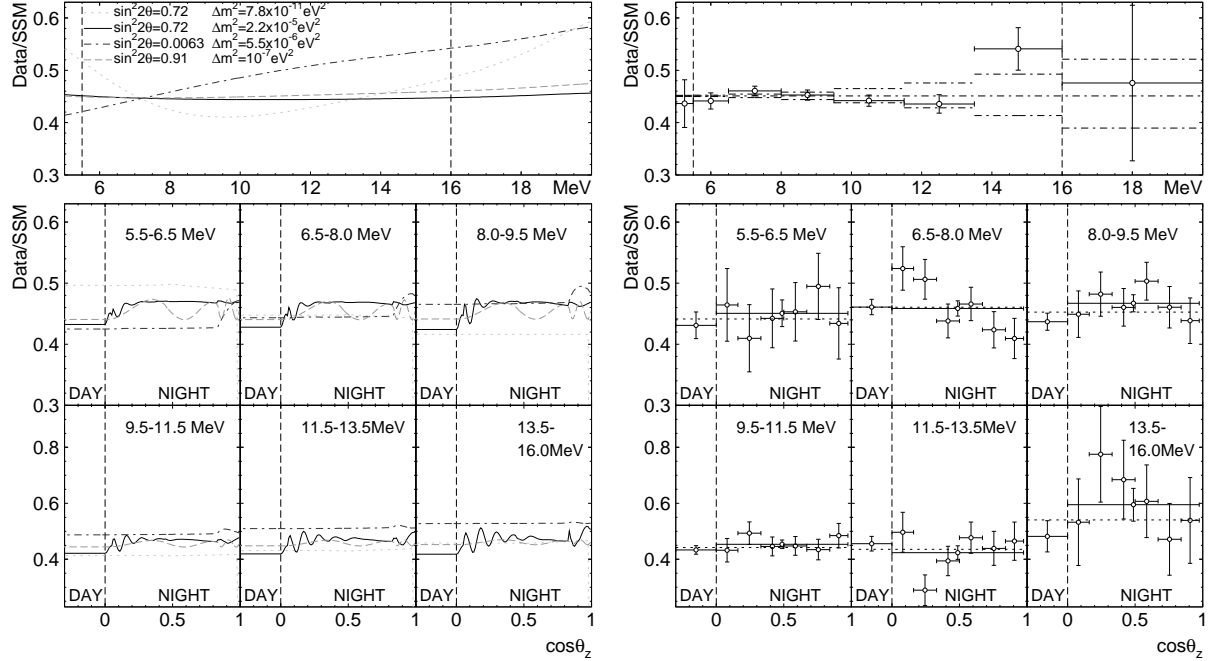


Figure 3: Predicted (left) and observed (right) spectral distortion (top) and zenith angle dependence (bottom) of the solar neutrino flux. The predictions are located in the LMA (solid), SMA (dashed-dotted), LOW (dashed) and VAC (dotted) region. The dashed-dotted lines in the right figure show the flux (45.1%) and the  $\pm 1\sigma$  energy-correlated systematic uncertainty. Due to a statistical limitation, the data sample is not broken into zenith angle bins for a recoil electron energy below 5.5 MeV and above 16 MeV. For the same reason, the displayed vertical axis interval is larger above 11.5 MeV.

There are several distinct two-neutrino oscillation solutions to the solar neutrino problem: The Large Mixing Angle (LMA) solution has a mass<sup>2</sup> difference  $\Delta m^2$  of about  $10^{-5}$  to  $10^{-4}$  eV<sup>2</sup> and a mixing angle in the range of  $\sin^2 2\theta = 0.4$  to 1. The Small Mixing Angle Solution (SMA) has a somewhat smaller  $\Delta m^2$  and mixing between  $10^{-3}$  and  $10^{-2}$ . The mixing at the LOW solution is close to maximal and the mass<sup>2</sup> difference is about  $10^{-7}$  eV<sup>2</sup>. Below  $10^{-9}$  eV<sup>2</sup> there are several VAC solutions where matter effects are unimportant. As shown in figure 3, LMA solutions show little spectral distortions, but have rapid oscillations of the flux as a function of zenith angle. The amplitude of these oscillations is larger for a larger recoil electron energy. Conversely, the high  $\Delta m^2$  part shows almost no zenith angle variation. The LOW solution has a small spectral distortion and slow oscillations of the flux as a function of zenith angle. The amplitude is larger for smaller recoil electron energy. A lower  $\Delta m^2$  will then suppress these oscillations. The SMA has moderate spectral distortion. There is almost no zenith angle variation in the mantle region, but there is enhancement (suppression) of the core flux at low recoil electron energy in the adiabatic (non-adiabatic) region. The VAC solutions typically have strong spectral distortion. The zenith angle variation is tiny (and due to a modified seasonal flux variation in conjunction with the correlation of season and zenith angle at SK’s geographic position). An explanation of the MSW zenith angle signatures can be found in<sup>9</sup>. The measured zenith angle spectrum is most consistent with flat, i.e. no spectral distortion and no zenith angle

dependence. It therefore favors high  $\Delta m^2$  LMA and low  $\Delta m^2$  LOW solutions as well as very small mixing SMA solutions in the non-adiabatic region, where the predicted spectral distortion is weak.

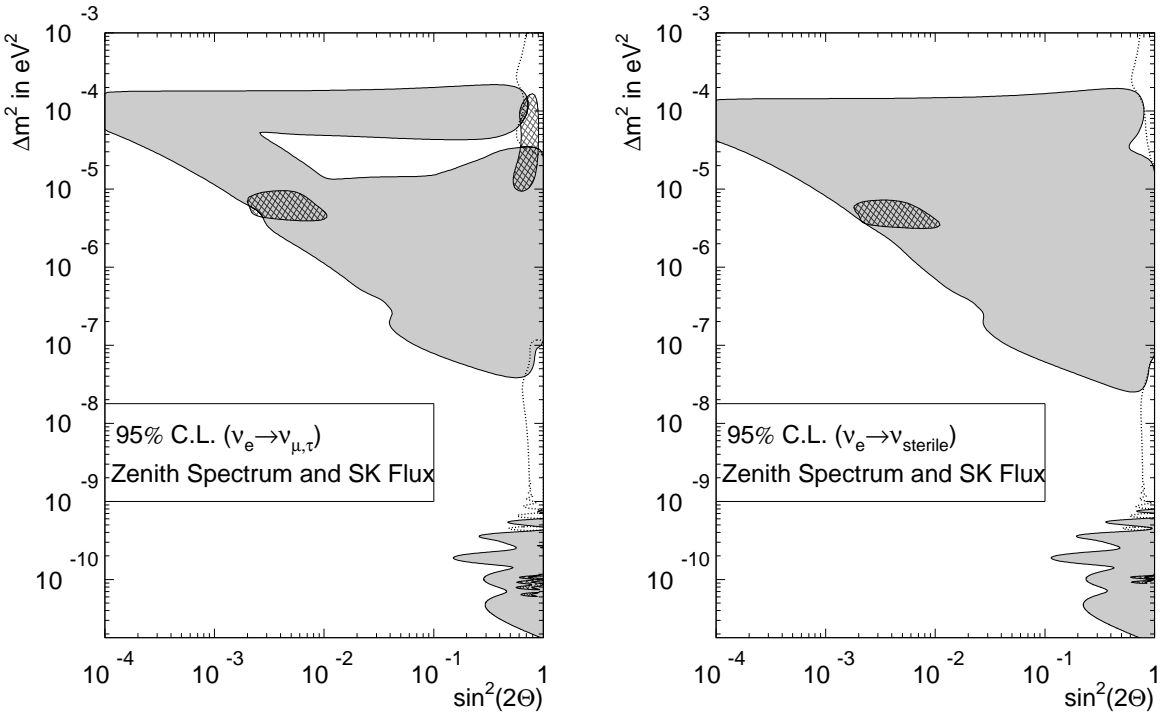


Figure 4: Excluded (grey areas) and allowed regions (dotted lines) for two-neutrino oscillation hypotheses. The figure on the left (right) assumes oscillations into only active (sterile) neutrinos. The excluded regions are based on an analysis of the zenith angle spectrum shape alone. The allowed areas use in addition the SK rate measurement. For comparison, the allowed areas based on the rates of Homestake<sup>1</sup>, GALLEX/GNO<sup>3</sup>, SAGE<sup>4</sup> and SK are overlaid.

A calculation of the zenith angle spectrum for each oscillation parameter was obtained as described in <sup>10</sup> for two cases: (i) oscillation into only active ( $\mu$ -type or  $\tau$ -type) neutrinos (ii) oscillation into only sterile neutrinos. As in <sup>10</sup> we define a  $\chi^2$  to compare prediction against data. A larger than expected flux from the *hep* branch of solar neutrinos can mimic the spectral distortion signature of neutrino oscillations. There is no *hep* flux uncertainty given in<sup>6</sup>. Therefore we search for the best-fit *hep* flux for each oscillation parameter set. The best-fit parameters are ( $\sin^2 2\theta = 1$ ,  $\Delta m^2 = 6.53 \cdot 10^{-10} \text{ eV}^2$ ) with 36.1/40 degrees of freedom (78.8% normalization factor and 0 *hep*) in the active and 35.7/40 degrees of freedom (91.7% normalization factor and 0 *hep*) in the sterile case. The shaded areas in figure 4 show 95% confidence level excluded regions based on this  $\chi^2$  minimum. Also seen in figure 4 are cross-hatched regions which represent 95% confidence level allowed regions (LMA, SMA and VAC) based on the measured rates of Homestake<sup>1</sup>, GALLEX/GNO<sup>3</sup>, SAGE<sup>4</sup> and SK<sup>5</sup>.

The best-fit zenith angle spectrum was searched for in these regions. (The LOW search region was for  $\sin^2 2\theta > 0.8$  and  $7.9 \cdot 10^{-8} \text{ eV}^2 < \Delta m^2 < 1.3 \cdot 10^{-7} \text{ eV}^2$ , the VAC region for  $\Delta m^2 < 10^{-8} \text{ eV}^2$ ) The zenith angle spectra are shown in figure 5. Only the LMA fit is truly inside the LMA region. The SMA (in the non-adiabatic region at the lower left corner) and LOW best-fits are at the boundary. The VAC best-fit point is at higher  $\Delta m^2$  than the regions shown in figure 4. The best-fit zenith angle spectra predict little spectral distortion or zenith angle variation. The residual spectral distortion of the best-fit SMA zenith angle spectrum leads to a low confidence level (about 7% from comparison with the  $\chi^2$  minimum).

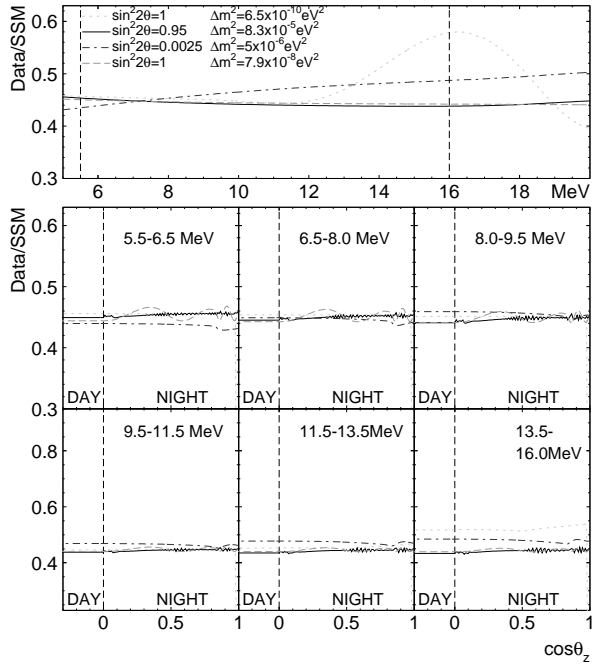


Figure 5: Best fit zenith angle spectrum for LMA (solid), SMA (dashed-dotted), LOW (dashed) and VAC (dotted).

We combined the night zenith angle bin and analyzed a day/night spectrum (eight energy bins, two zenith angle bins). Finally, we combined all zenith angle bins to search for spectral distortions only (eight energy bins). The resulting exclusion regions (95% confidence level) are shown in figure 6. The day/night spectrum expands the area excluded due to spectral distortion by a triangular region where a day–night asymmetry is predicted. Due to the zenith angle variation inside the night bin the zenith angle spectrum expands the excluded region further near the LOW and the LMA solutions. The non-adiabatic region of the SMA predicts a core suppression. It fits better with the zenith angle spectrum than either the spectrum or the day/night spectrum. This is due to a slightly smaller measured flux in the core bin compared to the day bin. Since the overall night flux exceeds the day flux, the day/night spectrum excluded area in this region is larger than that of the spectrum.

We also performed an analysis constraining the normalization factor within the BP2000 uncertainty. There is little change in best-fit point, normalization factor and *hep* flux. The  $\chi^2$  becomes 37.8/41 degrees of freedom in the active and 35.9/41 degrees of freedom in the sterile case. The region inside the dotted lines of figure 4 is allowed at 95% confidence level. In both the active and the sterile case, the 95% confidence level SMA and VAC regions are disfavored by the zenith spectrum shape at about 95% confidence level. The upper part of the LMA region is consistent with the zenith angle spectrum shape. The LMA region is missing in the sterile case (the sterile LMA cannot explain the difference between Homestake’s and SK’s rate by either spectral distortion or increased neutral current contribution to SK’s rate). SK data by itself (zenith spectrum and SK rate) result in two allowed areas at large mixing for either case. These areas are also shown in figure 7 at 99% confidence level. In the active case, three small areas appear at 99%; one at  $\sin^2 2\theta = 0.03$  to 0.1,  $\Delta m^2 = 2-4 \cdot 10^{-7} \text{ eV}^2$  in the MSW region and two which are close to the vacuum solution. No allowed region appears close to the small mixing angle solution. No new areas appear in the sterile case.

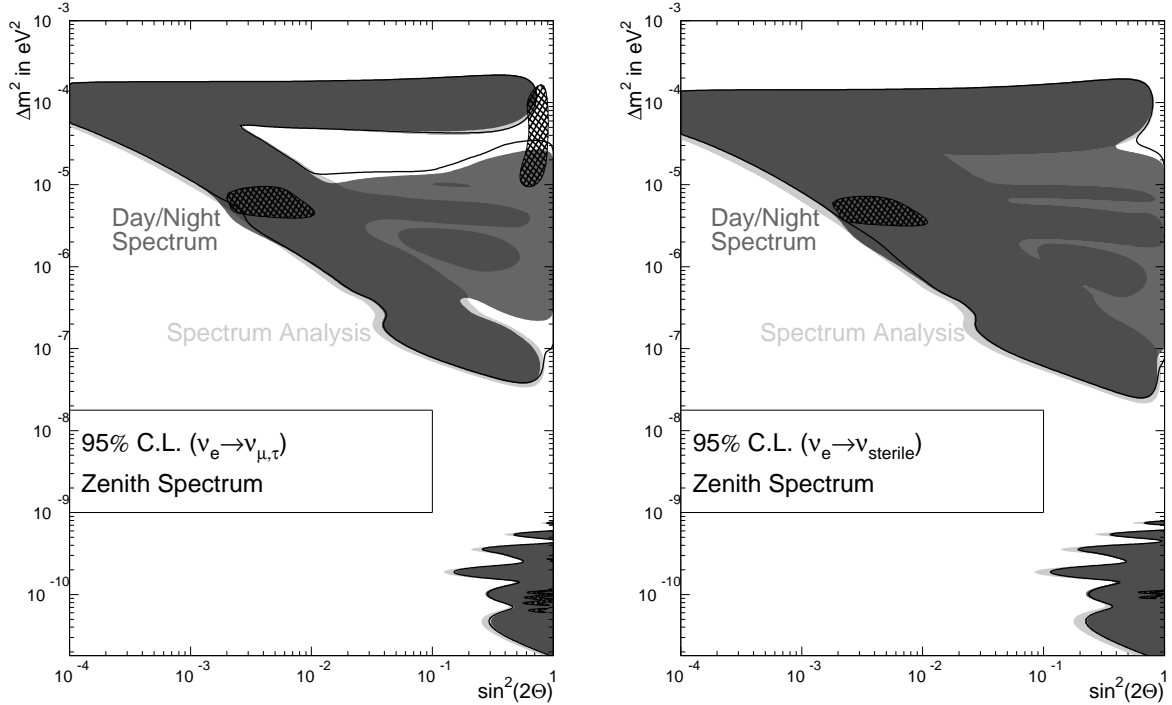


Figure 6: Regions excluded by the shape of the day/night spectrum (grey areas) and spectrum (light grey areas) in the active (left) and sterile (right) case. The dark grey area is excluded by both shapes. The inside of the solid line is excluded by the zenith angle spectrum shape (as in figure 4).

#### 4 Conclusion

With 1258 days of data, Super-Kamiokande has measured the  ${}^8\text{B}$  branch of the solar neutrino flux to be  $2.32 \pm 0.03(\text{stat})^{+0.08}_{-0.07}(\text{syst}) \times 10^6 / (\text{cm}^2 \text{s})$  and the  $\text{hep}$  branch to be less than  $40 \cdot 10^3 / (\text{cm}^2 \text{s})$  at 90% confidence level. No correlation of the neutrino flux with sunspot activity has been seen. The seasonal dependence of the neutrino flux favors the 7% modulation due to the eccentricity of the earth's orbit. No zenith angle dependence or distortion of the spectrum of the solar neutrino flux has been seen; the zenith angle spectrum is consistent with flat. In particular, the day-night asymmetry is  $A_{DN} = 0.033 \pm 0.022(\text{stat})^{+0.013}_{-0.012}(\text{syst})$ . The absence of zenith angle dependence and spectral distortion strongly constrains two-neutrino oscillations. From the six solution areas based on the rates of Homestake, GALLEX/GNO, SAGE and SK — active VAC, active SMA, active LOW, active LMA, sterile VAC and sterile SMA — all but active LMA are disfavored by the shape of the zenith angle spectrum at about 95% confidence level. Using only SK data (zenith angle spectrum shape and SK rate), two allowed areas (95% confidence level) at large mixing are found for the active as well as the sterile case:  $\Delta m^2 > 2-3 \cdot 10^{-5} \text{ eV}^2$  or  $10^{-9} \text{ eV}^2 < \Delta m^2 < 10^{-7} \text{ eV}^2$ .

#### Acknowledgments

The authors acknowledge the cooperation of the Kamioka Mining and Smelting Company. The Super-Kamiokande detector has been built and operated from funding by the Japanese Ministry of Education, Culture, Sports, Science and Technology, the U.S. Department of Energy, and the U.S. National Science Foundation. This work was partially supported by the Korean Research Foundation (BK21) and the Korea Ministry of Science and Technology.

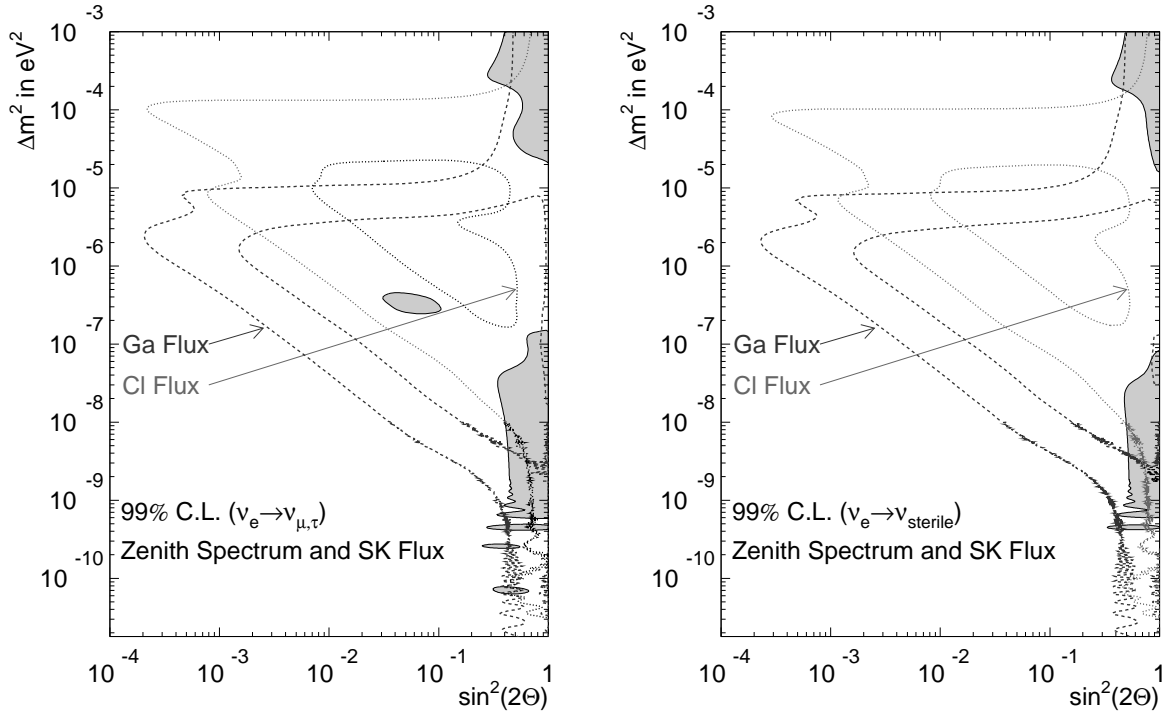


Figure 7: 99% confidence level allowed regions using all SK data (zenith spectrum and rate; grey areas) compared with GALLEX/GNO <sup>3</sup>+SAGE <sup>4</sup> (dashed line) and Homestake <sup>1</sup> (dotted line) for the active (left) and the sterile (right) case.

## References

1. B. T. Cleveland *et al.*, *Astrophys. J.* **496**, 505 (1998).
2. Y. Fukuda *et al.*, *Phys. Rev. Lett.* **77**, 1683 (1996).
3. E. Bellotti, *Nucl. Phys. B(Proc. Suppl.)* **91**, 44 (2001); W. Hampel *et al.*, *Phys. Rev. Lett.* **388**, 364 (1996); P. Anselmann *et al.*, *Phys. Lett. B* **342**, 440 (1995).
4. V. Gavrin, *Nucl. Phys. B(Proc. Suppl.)* **91**, 36 (2001); J.N. Abdurashitov *et al.*, *Phys. Lett. B* **328**, 234 (1994).
5. S. Fukuda *et al.*, *Phys. Rev. Lett.* **86**, 5651 (2001).
6. J. N. Bahcall *et al.*, astro-ph/0010346. The <sup>8</sup>B flux we have used is  $5.15 \times 10^6 \text{ cm}^{-2} \text{ s}^{-1}$  to be consistent with <sup>5</sup>. In this reference the <sup>8</sup>B flux has been updated to  $5.05 \times 10^6 \text{ cm}^{-2} \text{ s}^{-1}$ . This update does not change our conclusions.
7. Y. Fukuda *et al.*, *Phys. Rev. Lett.* **81**, 1562 (1998).
8. S. P. Mikheyev and A. Y. Smirnov, *Sov. Jour. Nucl. Phys.* **42**, 913 (1985); L. Wolfenstein, *Phys. Rev. D* **17**, 2369 (1978).
9. see for example A. J. Baltz and J. Wenner, *Phys. Rev. D* **50**, 5971 (1994) Q. Y. Liu, M. Maris, S. T. Petcov, *Phys. Rev. D* **56**, 5991 (1997) M. C. Gonzalez-Garcia, C. Peña-Garay, A. Yu. Smirnov, *Phys. Rev. D* **63**, 113004 (2001)
10. S. Fukuda *et al.*, *Phys. Rev. Lett.* **86**, 5656 (2001).